Structural and chemical investigation of $In_{0.6}Ga_{0.4}As$ Stranski-Krastanow layers buried in GaAs by transmission electron microscopy

A. Rosenauer, W. Oberst, D. Litvinov, and D. Gerthsen
Laboratorium für Elektronenmikroskopie, Universität Karlsruhe, Kaiserstrasse 12, D-76128 Karlsruhe, Germany

A. Förster and R. Schmidt
Institut für Schicht- und Ionentechnik, Forschungszentrum Jülich GmbH, Postfach 1913, 52425 Jülich, Germany
(Reveived 9 June 1999)

We report a detailed structural and chemical study of buried and free-standing $In_{0.6}Ga_{0.4}As$ Stranski-Krastanow islands. The layers were grown by molecular-beam epitaxy on GaAs(001) substrates. We investigated two different types of samples with nominal $In_{0.6}Ga_{0.4}As$ layer thicknesses of 1.5 and 2 nm. The growth was interrupted for 0, 60, or 180 s prior to the deposition of the 10-nm-thick GaAs cap layer. The chemical and structural analyses of the $In_{0.6}Ga_{0.4}As$ layers were carried out with high-resolution transmission electron microscopy. The chemical morphology of the buried layers was evaluated with the composition evaluation by lattice-fringe analysis (CELFA) method. The free-standing islands were investigated by strain state analysis combined with finite element calculations. The density and size distribution of the islands was obtained by conventional plan-view transmission electron microscopy. We found two types of islands: Coherent islands with a lateral size of approximately 13 nm and large islands (40–100 nm) showing plastical strain relaxation. The density of the defect-free small islands decreases with increasing duration of the growth interruption whereas the density and size of the large islands increases. A detailed study of the wetting layer with the CELFA method revealed about a 4-nm-thick $In_xGa_{1-x}As$ layer. The total amount of In contained in the wetting layer decreases with increasing duration of the growth interruption. Composition profiles in growth direction were measured. Their shape is explained by mainly three effects: Segregation of In, incorporation of migrating In into the growing cap layer, and strain-driven migration of In and Ga. An inhomogeneous In concentration increasing from bottom to top is observed in free-standing islands.

I. INTRODUCTION

Low-dimensional semiconductor heterostructures are at present one of the main research topics in solid-state physics. Most applications of semiconductor nanostructures are found in the field of optoelectronic devices like light-emitting diodes and lasers. The development of the quantum dot (QD) lasers is expected to lead to an increased quantum efficiency and to lower threshold-current densities.[1] In some high lattice-mismatch heterostructures such as $In_xGa_{1-x}As/GaAs$, the Stranski-Krastanow (SK) growth mode is observed that leads to the self-formation of QD's.[2,3] A simplified model that explains the occurrence of island formation in the SK growth mode is based on a balance of the surface energies of the substrate and the layer, the formation energy of the interface, the strain energy of the layer, and the deformation energy of the substrate. According to this model, the SK growth mode may occur for systems where the formation of a two-dimensional (2D) layer is favorable during the deposition of the first few monolayers (ML) of the layer. With increasing layer thickness, the strain energy of the 2D layer increases. Above a critical thickness $t_{c\,3D}$ the onset of island formation is observed mainly because an island offers the possibility of elastic strain relaxation at its free surfaces.[4] This model leads to a 2D wetting layer with 3D islands on its top. The elastic strain relaxation of the islands is incomplete, and plastic relaxation is observed if the island size exceeds a critical value that depends on the misfit between layer and substrate material, the island's shape, the composition distribution inside the island, elastic parameters, and the energy needed for the generation of the misfit dislocations. High-resolution transmission electron microscopy (HRTEM) investigations of the strain state of free-standing $In_{0.6}Ga_{0.4}As/GaAs(001)$ and InAs/GaAs(001) islands revealed[3] that the In concentration inside the islands is not homogeneous but increases from the bottom to the top of the island.

The simplified model explained above cannot be used to describe the density or size distribution of islands. For this purpose, kinetic models of 3D island nucleation have to be applied.[5] Experimental observations carried out by Ruvimov *et al.*[6] with photoluminescence spectroscopy (PL) and plan-view transmission electron microscopy report an equilibrium size of small (12–14 nm) InAs islands buried in GaAs grown by molecular-beam epitaxy (MBE). These equilibrium-size islands (that are stable during growth interruptions introduced prior to the cap layer growth) were only observed in a small window of an arsenic pressure of $p_0=(2\times10^{-6}\pm1\times10^{-6})$ torr at a growth temperature of 480 °C and a deposition of 4 ML InAs. For depositions between 2 and 3 ML InAs, the equilibrium islands could be formed by the introduction of a growth interruption between 10 s (3 ML) and 600 s (2 ML) prior to the deposition of the GaAs cap layer. At an As pressure of $p\geqslant3p_0$, strain-relaxed InAs clusters appear whereas the reduction to $p\leqslant1/3p_0$ leads to the formation of macroscopic 2D islands.

The main application of the $In_xGa_{1-x}As/GaAs$ SK struc-

tures is expected in the field of optoelectronic devices. From this point of view, the investigation of the local composition in buried SK layers becomes important. Commonly, PL and excitation spectroscopy are applied. These methods have the disadvantage that chemical and structural effects cannot be distinguished. Structural data obtained from free-standing islands by HRTEM or atomic force microscopy can be used for the interpretation of the optical data only if the SK layer is not altered during the capping. On the other hand, processes like the segregation of In into the GaAs cap layer have to be expected.[7] Here we focus on the investigation of the structure and local composition of $In_{0.6}Ga_{0.4}As$ SK islands in dependence of the nominal layer thickness and the duration of growth interruptions applied after the $In_{0.6}Ga_{0.4}As$ layer growth.

II. EXPERIMENTAL SETUP

The heterostructures were grown by MBE in a Varian Mod Gen II system on GaAs(001) substrates. The structures consist of a GaAs buffer layer and an $In_xGa_{1-x}As$ layer with a nominal In concentration of $x=60\%$. The overgrown samples contain a 10-nm-thick GaAs cap layer. Two sets of samples with nominal thicknesses of the $In_xGa_{1-x}As$ layer of 1.5 and 2 nm were grown. For each set, three capped samples with growth interruptions of 0, 60, or 180 s after the deposition of the $In_xGa_{1-x}As$ were available. Additionally, an uncapped sample was grown with an $In_xGa_{1-x}As$ layer thickness of 1.5 nm. The 0.1-μm-thick GaAs buffer layer was deposited at a substrate temperature of 600 °C while the temperature was reduced to 500 °C for the $In_xGa_{1-x}As$ and the GaAs cap layer growth. The GaAs ($In_xGa_{1-x}As$) growth rate was 1 μm/h (0.2 μm/h). The beam equivalent pressure V/III ratio was 22 (82) for the GaAs ($In_xGa_{1-x}As$) growth.

The transmission electron microscopy cross-section samples along the $\langle 100\rangle$ and $\langle 110\rangle$ projection were prepared conventionally. In the final stage, Ar^+- or Xe^+-ion milling was applied at an energy of 3 keV in a liquid-nitrogen-cooled specimen holder. Plan-view samples were prepared by dimple grinding and subsequent back-side chemical etching in a solution $1H_2O_2(30\%):5NaOH$. We used a Philips CM200 FEG/ST electron microscope with a spherical aberration constant of $C_S=1.2$ mm and a Scherzer resolution of 0.24 nm. Off-axis cross-section images used for the composition evaluation by lattice-fringe analysis (CELFA) method were recorded with an on-line charge coupled device (CCD) camera with 1024×1024 picture elements. The specimen tilt was $(3\pm1)°$ towards a $\langle 010\rangle$-zone axis. The HRTEM images for the strain state analyses were exposed in a $\langle 110\rangle$-zone axis orientation on photographic negative film. The negatives were digitized with an off-line CCD camera with 1024×1024 picture elements. Photoluminescence measurements were performed at a temperature of 2.6 K with an excitation density of 4 mW/cm^2 ($\lambda_{Ex}=517$ nm).

III. EXPERIMENTAL TECHNIQUES

A. Strain state analysis

The distribution of the strain and indium in the uncapped samples was investigated by the strain state analysis using the DALI program package.[8] This method is based on the measurement of local lattice distances and displacement vectors from HRTEM lattice images where the bright spots are correlated with the positions of atomic columns in the specimen. The bright intensity maxima positions will be further denoted as lattice positions although they are not necessarily located at the positions of atomic columns. Each local displacement vector is calculated as difference vector connecting an evaluated lattice position with its corresponding reference lattice position. The reference lattice is obtained by fitting an equally spaced reference lattice to the experimentally found lattice positions inside a reference region [see white frame in Fig. 1(a)]. Subsequently, the reference lattice is superimposed on the whole image.[8]

The idea behind the strain state analysis is based on the linear dependence of the local lattice parameter of a ternary material such as $In_xGa_{1-x}As$ on the local composition x according to Vegard's law:

$$a_{In_xGa_{1-x}As}=xa_{InAs}+(1-x)a_{GaAs}. \tag{1}$$

However, Eq. (1) only holds in bulk crystals. In pseudomorphically grown heterostructures, the tetragonal distortion has to be taken into account. A further handicap is the small thickness of the HRTEM specimens in the range of 5 to 20 nm. For small thicknesses, the effects of surface stresses could gain importance. They arise from a tendency of the surface atoms to achieve an in-plane lattice parameter different from that in the bulk. Throughout this paper we assume that this effect is negligible because it concerns only a negligible fraction of atoms even for the smallest specimen thicknesses of about 5 nm. The most important effect of the small specimen thickness is an elastic relaxation of the strained layer in the vicinity of the specimen surfaces. For sufficiently thin specimens, the biaxial strain state of the bulk sample is reduced to the uniaxial case. In practice, the specimen thickness often lies between these limiting cases of an infinitely thin or thick sample, and an analytical solution of the strain state of the specimen is only known for layers with laterally homogeneous composition.[9] In the case of free-standing islands, finite element (FE) calculations have to be performed with a three-dimensional FE model according to the specimen geometry that is visible in the HRTEM lattice image. An important parameter is the local sample thickness in electron-beam direction that is evaluated from the HRTEM image according to the quantitative analysis of the information fromthe transmission electron micrographs (QUANTITEM) procedure.[10–12] The composition distribution inside the island is guessed in a first approximation, and the subsequent calculation yields the displacements at the nodes of the finite elements [see Fig. 1c]. To be able to compare these results with the experimentally evaluated displacements, a 3D atomic model is generated with local lattice parameters according to the result of the FE simulations. The displacement of each atom is calculated from an interpolation of the displacements of neighboring FE nodes. In order to approximately take into account the TEM imaging process, atomic displacements are averaged along columns of atoms corresponding to the electron-beam direction in the TEM. The resulting 2D grid of projected columns is evaluated in analogy to the experimental image. The simulated

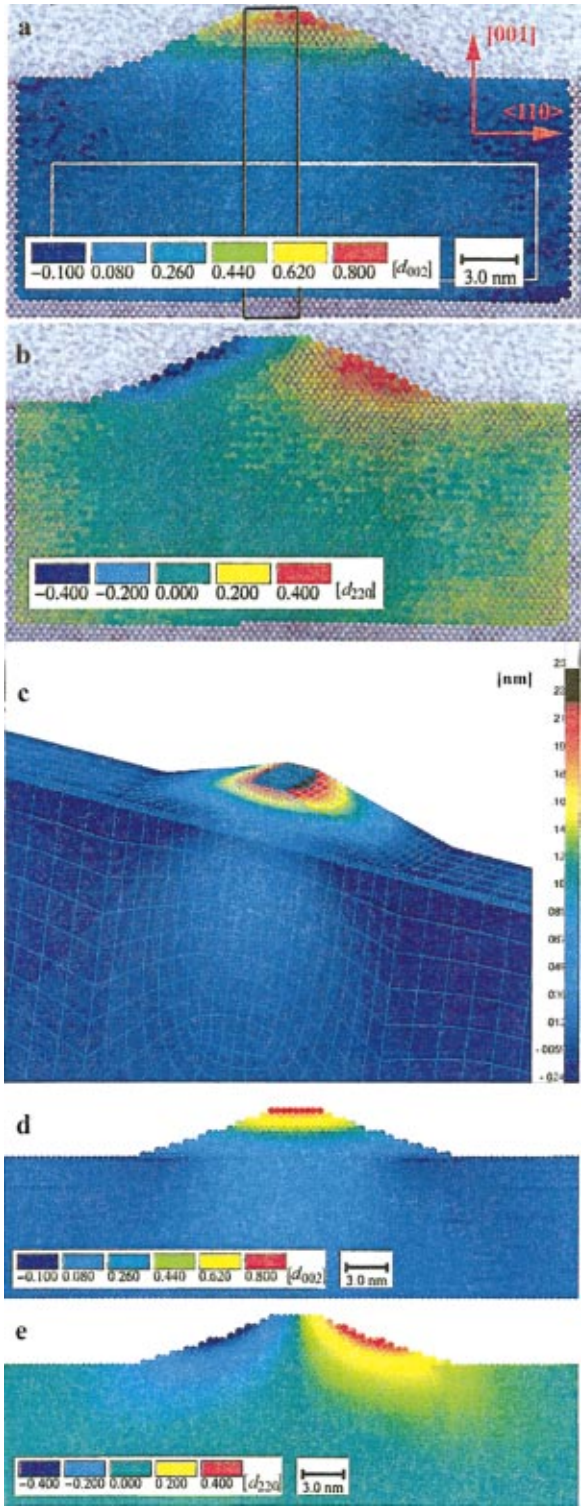

FIG. 1. (Color) (a) Color-coded map of local displacements in growth direction evaluated from an ⟨110⟩-HRTEM image of an uncapped sample with an $In_xGa_{1-x}As$ layer thickness of 1.5 nm. The displacement values shown in the legend are normalized with respect to the averaged distance d_{002} of the horizontal (002)-lattice planes inside the reference region that is marked with a white frame. The black frame marks the area that was used to adapt FE simulated and experimental displacements. (b) Components of the displacement vectors parallel to the interface of the same area. The displacement values are normalized with respect to the averaged distance d_{220} of the vertical (220)-lattice planes inside the reference region. (c) Finite element model with color-coded displacements in growth direction. The light blue grid indicates the finite elements. (d) 2D color-coded map of simulated displacements in growth direction obtained from the projection of a 3D atomic model in electron-beam direction. The 3D atomic model was generated according to the FE results shown in (c). (e) Color-coded map of simulated displacements parallel to the interface.

displacements are then compared with the experimental ones. Deviations give information about deviations between the guessed and real In distribution in the island. In an iterative process, simulated and experimental displacements are adapted. A detailed description of the applied procedures was published by Rosenauer *et al.*[3,8,10,13] To summarize, the evaluation of the In concentration is performed in the following steps.

(1) Evaluation of displacements from the HRTEM image with the DALI program package. Calculation of a displacement profile in growth direction by averaging along (002) planes running parallel to the interface plane in a region as marked with a black frame in Fig. 1(a).

(2) Evaluation of the local sample thickness according to the QUANTITEM method.

(3) Generation of a 3D FE model with a guessed In concentration distribution inside the island and in the wetting layer.

(4) FE calculation.

(5) Generation of a 3D atomic model with displacements calculated from the FE results.

(6) Averaging of atomic displacements along columns in

electron-beam direction yielding a 2D model of projected atomic positions.

(7) Evaluation of the 2D model analogously to item (1).

(8) Comparison of simulated with experimental displacements. If necessary, changes of the concentration distribution inside the island and in the wetting layer are performed and the process is continued with item (4).

B. Composition evaluation by lattice-fringe analysis

The local composition of the capped samples was investigated with the CELFA method that is briefly outlined in this section. It is well known that an electron wave that interacts with a crystalline sample is diffracted resulting in the formation of Bragg diffraction spots that are observed in the back focal plane of the objective lens. Theoretically, dynamical diffraction can be described in the scope of the Bloch wave theory. Each reflection is defined by its complex amplitude $F_{hkl}=a_{hkl}e^{ip_{hkl}}$, where a_{hkl} is the (real) amplitude and p_{hkl} the phase. Most of these reflections depend on the composition of the diffracting crystal. In the kinematic approximation, F_{hkl} is proportional to the structure factor S_{hkl}, that is, for the sphalerite-type $In_xGa_{1-x}As$ crystal, given by

$$S_{hkl}=4[f_{In_xGa_{1-x}}+f_{As}e^{i2\pi(h+k+l)/4}], \tag{2}$$

where the f are the atomic form factors. Here we find that the $\{020\}$ reflections show the strongest dependence on the composition because

$$S_{020}=f_{In_xGa_{1-x}}-f_{As}. \tag{3}$$

It can be shown by simulations that S_{020} vanishes for an In concentration of $x=0.22$. An advantage of the $\{020\}$ reflections is that they cannot be excited by multiple scattering in the vicinity of the $\langle 100\rangle$-zone axes. The most simple way to exploit the chemical sensitivity of a $\{020\}$ reflection in TEM is the use of a single-beam dark-field imaging condition with the $\{020\}$ beam centered on the optic axis and a crystal orientation with only the $\{020\}$ and the central beam being strongly excited. The centering is necessary to minimize the effects of objective lens aberrations that vanish on the optic axis. The single-beam dark-field imaging has the following disadvantages. First, the noise in the image is rather high, which is mainly due to amorphous surface layers of the TEM specimen limiting the accuracy of a local composition evaluation. Second, variations of the image intensity may be due to variations of the specimen thickness or/and due to a variation of the chemical composition. Additionally, an ambiguity of the intensities occurs. Figure 2 shows the image intensity for various specimen thicknesses plotted versus the composition x. The curves were calculated with the Bloch wave method using the EMS program package.[14] The intensities are normalized with respect to the intensity in binary GaAs. Although the shape of the curves is similar up to a specimen thickness of 50 nm, In concentrations $x_1=0.22+\Delta x$ and $x_2=0.22-\Delta x$ yield similar image intensities. The third disadvantage is the background intensity that is supplied by the inelastically scattered electrons. The result is, for example, that the image intensity does not vanish for an In concentration of $x=0.22$.

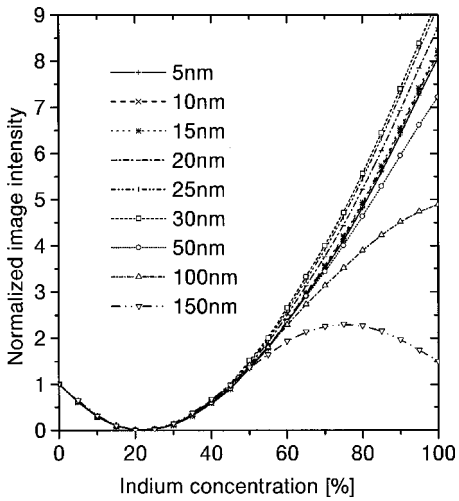

FIG. 2. Image intensity plotted versus the In concentration for various specimen thicknesses in electron-beam direction. The intensity is normalized with respect to GaAs. The curves were calculated according to an imaging condition where only the (002) and the (000) beams are strongly excited.

The CELFA method uses an imaging condition where the (040) and the central beam are strongly excited. Again, the (020) beam is centered on the optic axis. The interference of the three beams produces a fringe pattern. The first advantage of a periodic image is that it allows noise filtering.[8,13] Second, the effect of inelastically scattered electrons is reduced because they are not coherent. For the evaluation of the local In concentration, we use the local amplitude and phase of the (020) reflection in the Fourier-transformed image, which can be obtained in two different ways. First, the image, can be subdivided into image unit cells. Each unit cell has a size of 2 ML$\times$2 ML. In the Fourier-transformed cell, the amplitude of the (020) reflection is measured.[13,15,16] The second possibility consists of the Fourier transform of the whole image.[17] A circular area around the (020) reflection is chosen. The information outside the circle is deleted, and the information inside the circle is centered in such a way that the pixel with largest intensity of the power spectrum lies on the zero-frequency position in Fourier space. The inverse Fourier transformation provides spatially resolved information on the amplitude A_{020} and phase P_{020} of the (020) reflection. In both cases, the measured amplitude A_{020} of the (020) reflection contains information on the amplitude a_{020} of the chemically sensitive (020) beam, because

$$A_{020}\propto a_{020}\sqrt{a_{000}^2+a_{040}^2+2a_{000}a_{040}\cos(\phi_n)}, \tag{4}$$

where the phase ϕ_n depends on the phases of the involved beams and furthermore is a linear function of the objective lens defocus Δf. Note that the amplitude A_{020} that is measured in the Fourier-transformed image is not equal to the amplitude a_{020} of the (020) beam of the diffracted electron wave because A_{020} in Eq. (4) results from the interferences of the (020) beam with the (000) and the (040) beam. Here the ambiguity of the intensities that occurs in the single-beam dark-field imaging can be solved because the phase P_{002} differs by π for regions with compositions below and above $x=0.22$. In Refs. 13, 16, and 17 it was shown, that the specimen thickness in electron-beam direction can be estimated

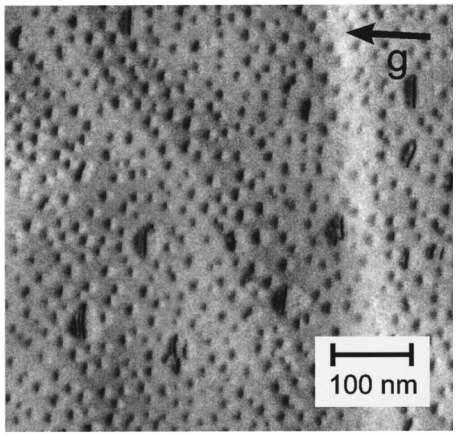

FIG. 3. Plan-view **g**/3**g** weak beam image with $\mathbf{g}=\langle 220\rangle$ of the uncapped sample with an $In_xGa_{1-x}As$ layer thickness of 1.5 nm.

from Eq. (4), if a defocus series is taken instead of only one image. Furthermore, variations of the specimen thickness and of the imaging parameters over the image can approximately be taken into account. For a detailed description of the implemented procedure, see Refs. 13, 16, and 17.

IV. EXPERIMENTAL RESULTS

A. Uncapped sample

In this section we present the experimental results of the uncapped sample with an $In_xGa_{1-x}As$ layer thickness of 1.5 nm. Figure 3 depicts a plan-view weak beam image. It shows two types of islands. We find coherent small islands with a lateral size of 16 ± 3 nm as well as approximately 50 nm large islands that contain misfit dislocations. The density of the coherent islands is 1.5×10^{11} cm^{-2} and that of the large strain relaxed islands is 2.7×10^{9} cm^{-2}.

HRTEM images revealed an average lateral size of the coherent islands of $l=13.3\pm1.5$ nm and a height h of 2.8 ± 0.4 nm. The values are obtained from the evaluation of 15 islands. The errors are calculated from the standard deviation. The aspect ratio l/h of the islands is 4.8 ± 0.4.

Figures 1(a)and 1(b) show the DALI evaluation of a HRTEM image of a coherent island. The evaluated local displacement vectors are decomposed into two perpendicular components. Figure 1(a) displays a color-coded map of the component in growth direction. Figure 1(a) clearly shows that the displacements (their mean value vanishes inside the reference region) increase from the bottom to the top of the island revealing an enlarged lattice parameter compared to the GaAs buffer. The black frame marks the area that was used to average the local displacements along the horizontal (002) planes yielding the displacement profile in growth direction that is shown in Fig. 4 (solid circles). Note that the displacements near the surface beside the island does not yield substantial indications for a wetting layer. Figure 1(b) shows the components of the local displacement vectors parallel to the interface. The red regions correspond to displacement vectors pointing to the right, and the blue region corresponds to those pointing to the left. Both regions result from the relaxation of the elastic strain of the island that results in a displacement of atoms near the island's surface in outward direction.

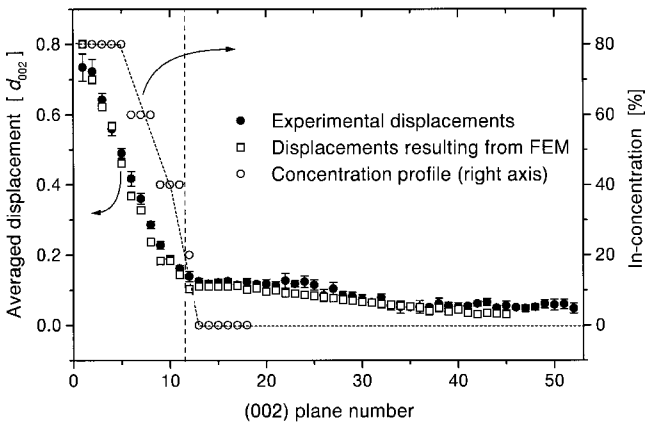

FIG. 4. Experimentally measured and FE simulated averaged displacements plotted versus the (002)-plane number. The displacements were averaged in regions corresponding to the black frame in Fig. 1(a). The open circles show the concentration profile that was used for the FE calculation. The vertical dashed line indicates the position of the surface beside the island.

Figure 1(c) shows the finite element model that was generated according to the island shape and the local sample thickness measured with the QUANTITEM (Ref. 10–12) procedure. It should be mentioned that the local specimen thickness could only be evaluated in the GaAs buffer because the HRTEM contrast pattern also depends on the In concentration. Figure 5 is a plot of the specimen thickness, used for the FE modeling, revealing a wedge-shaped specimen. The angle of the wedge is 26°. This specimen shape is in good agreement with the TEM sample preparation conditions. Two Ar^+-ion guns were applied under an angle of 15° from which we expect a 30° wedge. As shown in Fig. 5, the specimen thickness in the island region is extrapolated from the values measured in the GaAs buffer.

Figure 4 contains the concentration profile that leads to the best agreement of measured and simulated averaged displacements that are also shown in Fig. 4. The concentration profile shows four steps because the FE model of the island and the wetting layer was subdivided into five solids. The In

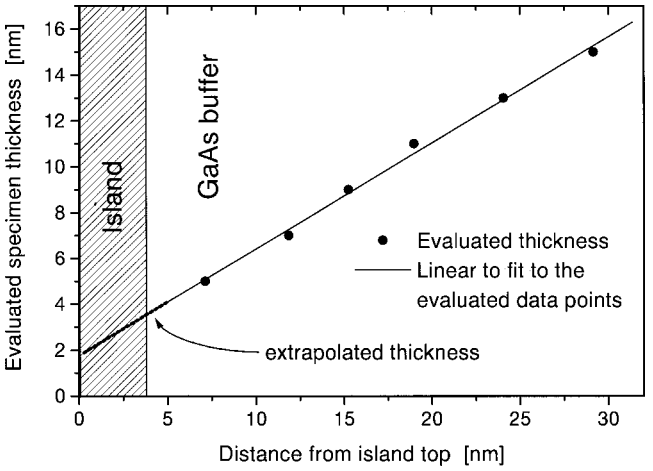

FIG. 5. Evaluated specimen thickness plotted versus the distance from the island top parallel to the growth direction. The specimen thickness in the region of the island is extrapolated from the GaAs buffer.

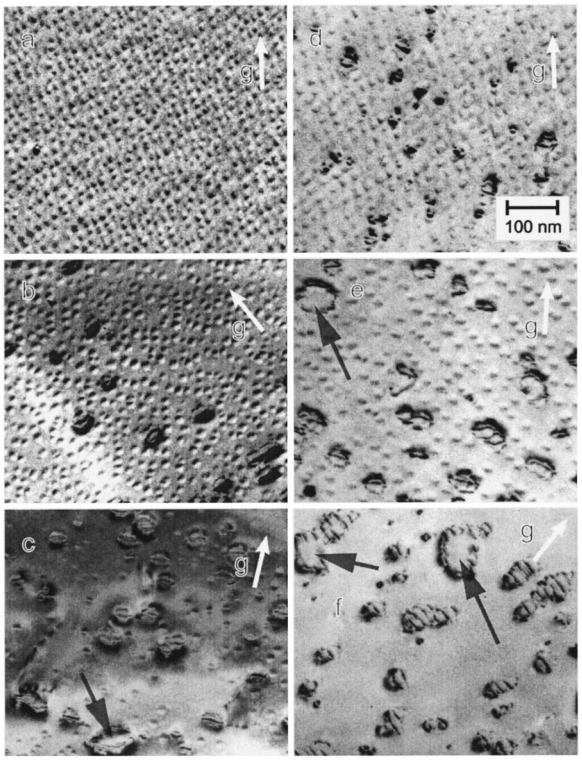

FIG. 6. TEM plan-view micrographs from capped samples obtained under a **g**/3**g** weak beam condition with **g**=⟨220⟩. Micrographs (a), (b), and (c) correspond to an $In_xGa_{1-x}As$ layer thickness of 1.5 nm and (d), (e), and (f) to a thickness of 2 nm. The duration of the growth interruption is 0 s for (a) and (d), 60 s for (b) and (e), and 180 s for (c) and (f). The dark arrows mark islands with missing strain or dislocation contrast in the center.

concentration is homogeneous inside each solid. The profile shows only four steps because the two solids next to the top of the island have the same In concentration. From the position of the surface beside the island, we estimate a thickness of the wetting layer of roughly 1 ML (see vertical dashed line in Fig. 4).

To be able to compare the strain fields of the entire FE model with the experiment, the 2D model of projected atom columns (see Sec. III A) was evaluated analogously to the experimental image. The result is shown in Figs. 1(d) and 1(e). Obviously, the evaluated In concentration profile leads to good agreement with the experimental displacement vectors shown in Figs. 1(a) and 1(b).

B. Capped samples

1. Structural properties

(a) *TEM plan view.* Figure 6 shows weak beam plan-view micrographs of all investigated samples that contain a 10-nm-thick GaAs cap layer. Similarly to the uncapped sample, we find two types of islands: Coherent islands with a size of approximately 15 nm and strain-relaxed islands that reach a lateral extension of about 100 nm for the longest duration of the growth interruption. From Fig. 6 it becomes obvious that the small coherent islands are not stable. For both $In_xGa_{1-x}As$ layer thicknesses of 1.5 and 2 nm, the density of the coherent islands decreases with increasing duration of the

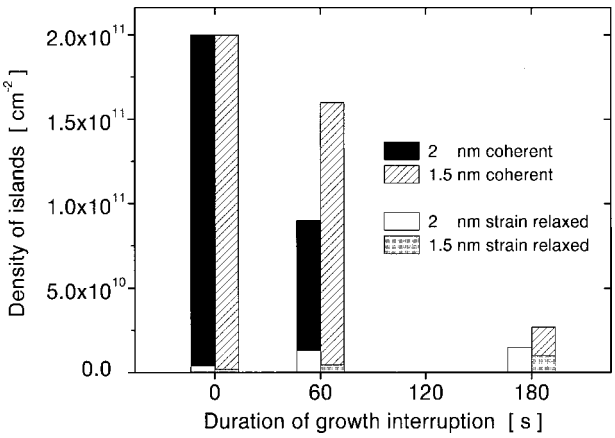

FIG. 7. Density of investigated capped islands plotted versus the duration of the growth interruption.

growth interruption. The density of the large strain-relaxed islands inversely depends on the duration of the interruption. We did not observe any coherent islands in the 2 nm sample with a growth interruption of 180 s.

Figure 7 gives a survey of the island densities. It reveals that the densities of relaxed islands are significantly larger for the 2 nm samples. Furthermore, one clearly recognizes that the density of the coherent islands drops more quickly in the 2 nm samples. In this context it is important to note that the initial density of coherent islands was equal for both $In_xGa_{1-x}As$ layer thicknesses. Therefore, we deduce that the initial coherent islands are more stable in the 1.5 nm sample than in the 2 nm sample. This result will be important later on.

(b) *Photoluminescence spectroscopy.* The low stability of the islands in the 2 nm sample is also visible in the PL spectra shown in Fig. 8. Here we find that the position of the QD emission line is approximately stable at 1.173 eV for the 1.5 nm sample. In the 2 nm sample, we find a significant blue shift from 1.113 eV (0 s) to 1.155 eV (60 s). Additionally, the full width half maximum (FWHM) of the PL curve of the 60 s sample is increased.

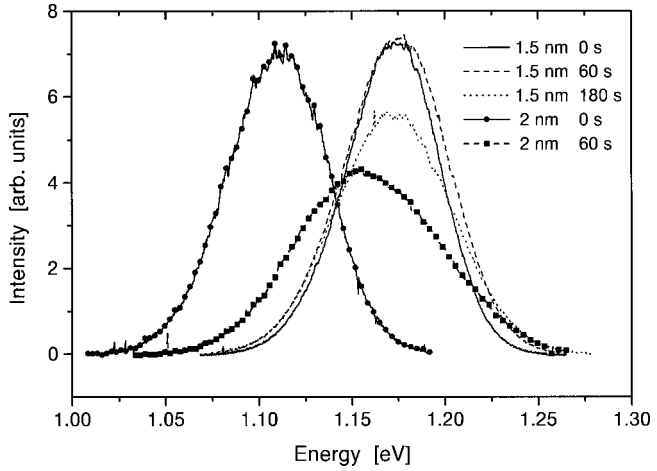

FIG. 8. Low-temperature PL spectra showing the emission from QD's. The sample with 2 nm layer thickness and 180 s growth interruption did not show any QD emission.

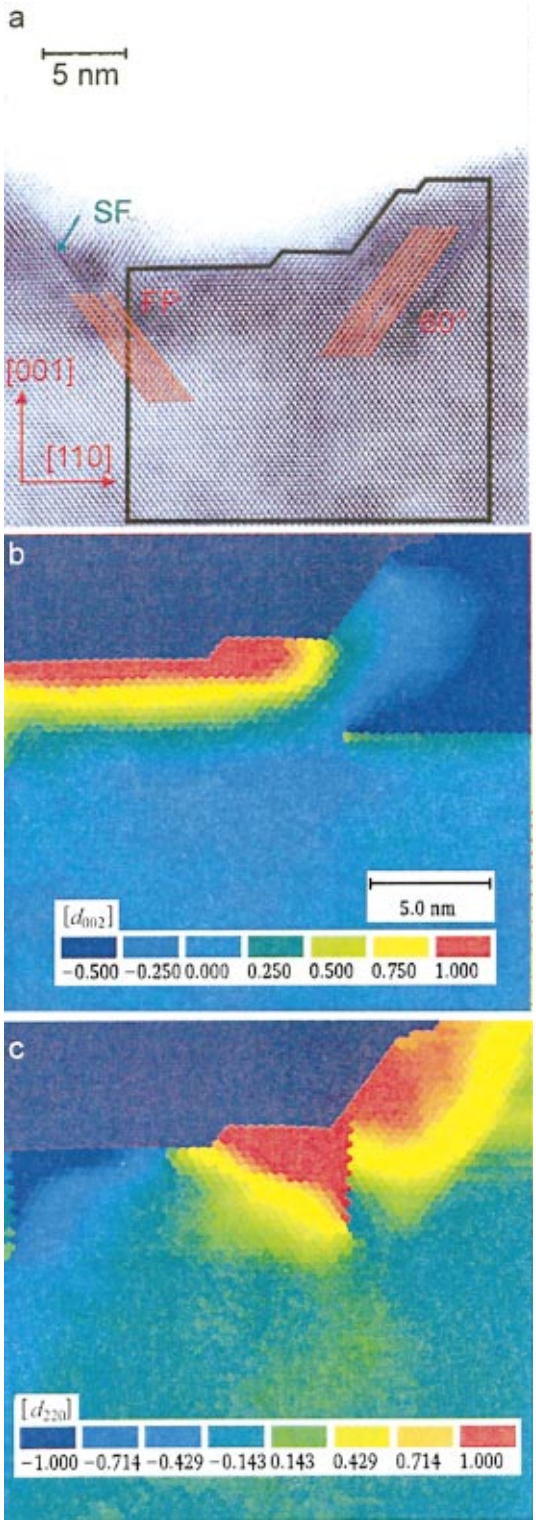

FIG. 9. (Color) (a) HRTEM micrograph of the sample with 2 nm $In_xGa_{1-x}As$ layer thickness taken in $[\bar{1}10]$-zone axis orientation showing an island with missing cap layer. The island contains a Frank-partial dislocation (FP) and a 60° dislocation. The red lines help to identify terminating $\langle 111\rangle$-lattice planes of the substrate. The black frame indicates the region that was evaluated by strain state analysis. The color-coded maps (b) and (c) show local displacement vector components in growth direction and in interface direction, respectively. The reference region was chosen inside the GaAs buffer. In (c), the abrupt transition from green to blue and from red to green occurring along two vertical lines at the left and right side of the island, respectively, are due to (220)-lattice fringes of the substrate that end at the dislocation cores. The red region corresponds to displacement vectors pointing to the right and the blue regions to those pointing to the left.

2. Islands with interrupted cap layer

In Fig. 6 we find some large islands with dislocations that are rather conspicuous (marked with dark arrows) because the strain and dislocation contrast vanishes in an approximately circular area around the island center. Such islands mainly occur in the 2 nm samples for 60 and 180 s growth interruptions. In corresponding HRTEM images, we find islands with missing cap layers on their tops at a similar density. One of them is displayed in Fig. 9(a). The imaged crystal region contains two misfit dislocations with terminating $\{111\}$-lattice planes of the substrate.

Figure 9(b) shows the components $u_\perp$ of the displacement vectors in growth direction evaluated from the HRTEM image in Fig. 9(a) (inside the region indicated by a black frame). The sharp transition from green ($u_\perp \approx +0.5$) to blue ($u_\perp \approx -0.5$) along a horizontal line in the right part of the image is due to a missing (002)-lattice plane terminating at the misfit dislocation. In the left part of the image, the increasing $u_\perp$ clearly supplies evidence for the existence of an

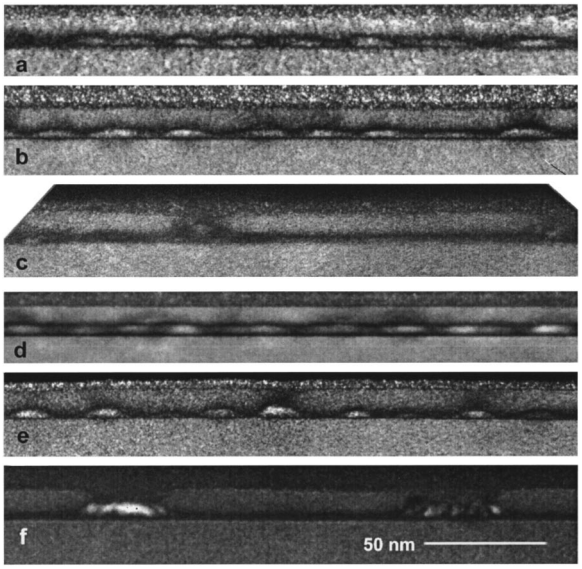

FIG. 10. Conventional single-beam dark-field images obtained with the strongly excited (002) beam on the optical axis. (a), (b), and (c) show the results for the sample with 1.5 nm $In_xGa_{1-x}As$ layer thickness and (d), (e), and (f) those for the 2 nm sample. The duration of the growth interruption is 0 s for (a) and (d), 60 s for (b) and (e), and 180 s for (c) and (f). The corresponding In concentration can be roughly estimated from Fig. 2.

$In_xGa_{1-x}As$ island reaching from the interface to the top of the visible contrast pattern in Fig. 9(a). Hence, the GaAs layer is completely missing at the top of the island. A profile of $u_\perp$ along the growth direction, that was averaged inside a narrow area positioned at the center of the red region in Fig. 9(b), reveals a lattice parameter in growth direction of $a_\perp = 1.094 a_{GaAs}$ close to the top of the island (a_{GaAs} is the bulk lattice parameter of GaAs). Now we assume that the center of the island is fully strained as can be verified from Fig. 9(c) where the displacement vector components in interface direction vanish in the island center. Then, the corresponding bulk-material lattice parameter a is calculated according to[13]

$$\frac{a_\perp - a_{GaAs}}{a_{GaAs}} = \alpha \frac{a - a_{GaAs}}{a_{GaAs}}. \tag{5}$$

The parameter α depends on the degree of the elastic relaxation in electron-beam direction. Assuming that the island top region is completely strain relaxed in electron-beam direction, we obtain[13] $\alpha \approx 1.5$ yielding $(a - a_{GaAs})/a_{GaAs} \approx 0.063$, which corresponds to an In concentration of approximately 90%.

3. Evaluation of the chemical composition

In this section we present the evaluation of the chemical composition of the capped samples by the exploitation of the chemically sensitive {020} reflections.

(a) *Conventional dark-field imaging.* Figure 10 shows single-beam dark-field images obtained with a strongly excited (002) reflection. It is appropriate to note that this means a diffraction of the electron beam by the (002)-lattice planes occurs parallel to the interface plane. Therefore, the electron beam is parallel to the interface plane in a very good approximation and the visible $In_xGa_{1-x}As$ region does not contain any blurring induced by a crystal tilt. Although it was mentioned in the preceding that these kinds of images can hardly be evaluated quantitatively, they provide a good survey over the In concentration in regions with a lateral expansion of several hundreds of nm. We deduce from Fig. 2 that the darkest regions of the $In_xGa_{1-x}As$ layer correspond to an In-concentration of approximately 22%. Regions with a brightness comparable with the GaAs have an In concentration of 40%. Therefore, the dark stripe with the bright dots corresponds to a quantum well with an In concentration below approximately 30% containing islands with an In concentration of approximately 40% or larger. Note that the given concentrations are only roughly estimated.

As expected from the plan-view images, the density of coherent islands decreases with increasing duration of the growth interruption. No coherent island is found in the sample with 2 nm $In_xGa_{1-x}As$ layer thickness and a growth interruption of 180 s. Instead, large islands are observed that frequently exhibit a tangled contrast caused by dislocations. Figure 10(f) (2 nm and 180 s growth interruption) contains one of the rare islands that appear to be dislocation free in the center part. Note that the cap layer is interrupted on top of the island.

The most striking result that becomes apparent from Fig. 10 is a siginificant transformation of the $In_xGa_{1-x}As$ layer morphology by the GaAs overgrowth. The initially 1- or 2-ML-thick wetting layer is significantly broadened so that islands and wetting layer now have similar extensions in growth direction. Therefore, the initial $In_xGa_{1-x}As$ layer consisting of a thin wetting layer and 3D islands has been transformed into an approximately 4-nm-thick quantum well (QW) with low In concentration that contains inclusions with larger concentrations.

(b) *Composition evaluation by lattice-fringe analysis.* The investigation of the local composition of the capped layers was performed with the CELFA method. In order to avoid effects of different lattice parameters on the observed contrast pattern, the samples were oriented in such a way that the (020)-lattice fringes perpendicular to the interface plane are chosen for the evaluation. These lattice fringes have the same lattice parameter in a good approximation in regions where the $In_xGa_{1-x}As$ layers were grown pseudomorphically. For that purpose, the samples were tilted approximately 3° around an axis running parallel to the interface plane and perpendicular to the electron-beam direction. Note that this sample orientation induces a small but not significant blurring of the interfaces. However, this effect will be taken into account for the quantitative evaluations presented in the discussion.

Figure 11 shows the resulting color-coded maps of the local In concentration. Each colored square covers an area of $a_{GaAs} \times a_{GaAs}$. Figure 11 clearly reveals the existence of a broad wetting layer with a maximum In concentration x that decreases with increasing duration of the growth interruption. The wetting layer contains inclusions with enlarged In concentration with a lateral size of approximately 13 nm. For samples with 0 and 60 s growth interruption, the maximum measured In concentration is 40% in the 1.5 nm samples and 48% in the 2 nm samples. Small coherent islands are also found in the 1.5 nm sample with 180 s growth interruption.

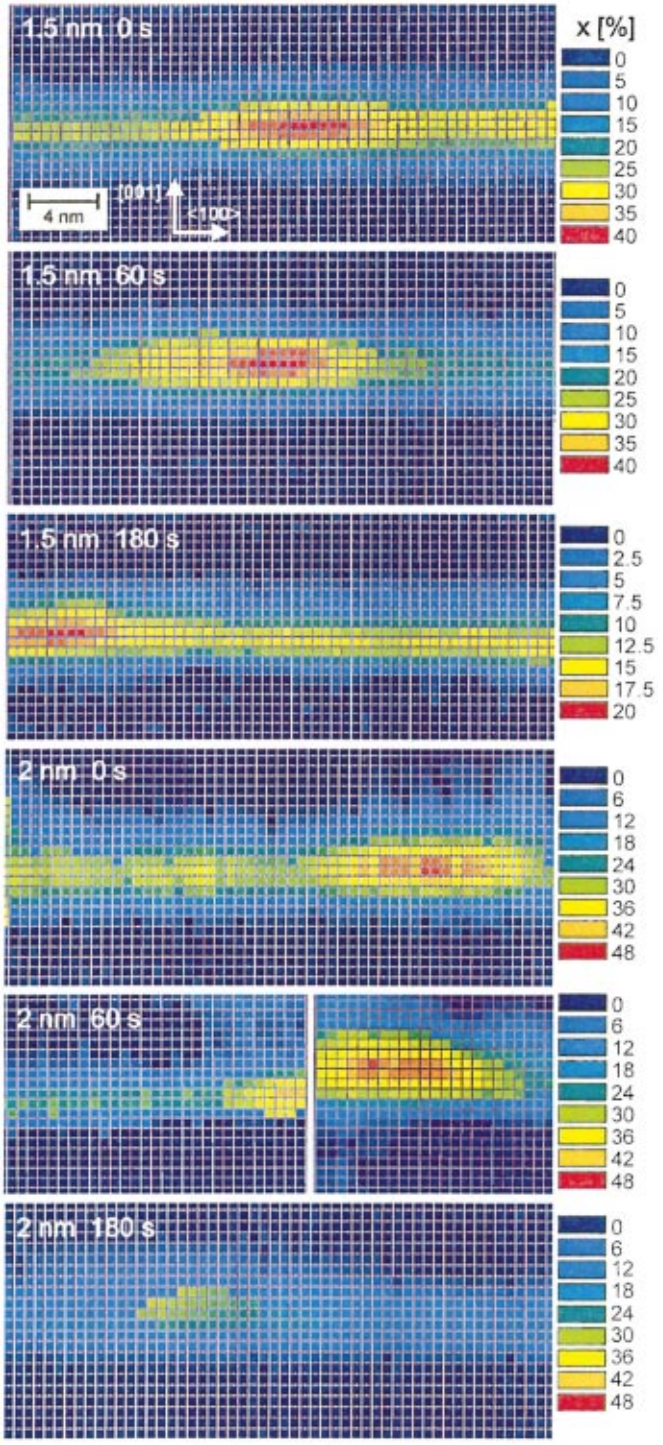

FIG. 11. (Color) Color-coded maps of the local In concentration x evaluated with the CELFA method. Note that the color encoding is not identical for all maps.

They show a maximum In concentration of approximately 18%. Note that the In concentration that is measured in the island regions is smaller than the real In concentration inside the buried island if the sample thickness in electron-beam direction is larger than the island's extension.

Figure 12 shows concentration profiles in growth direction obtained from the wetting layers of all investigated samples. One clearly recognizes that the maximum In concentration decreases with increasing duration of the growth

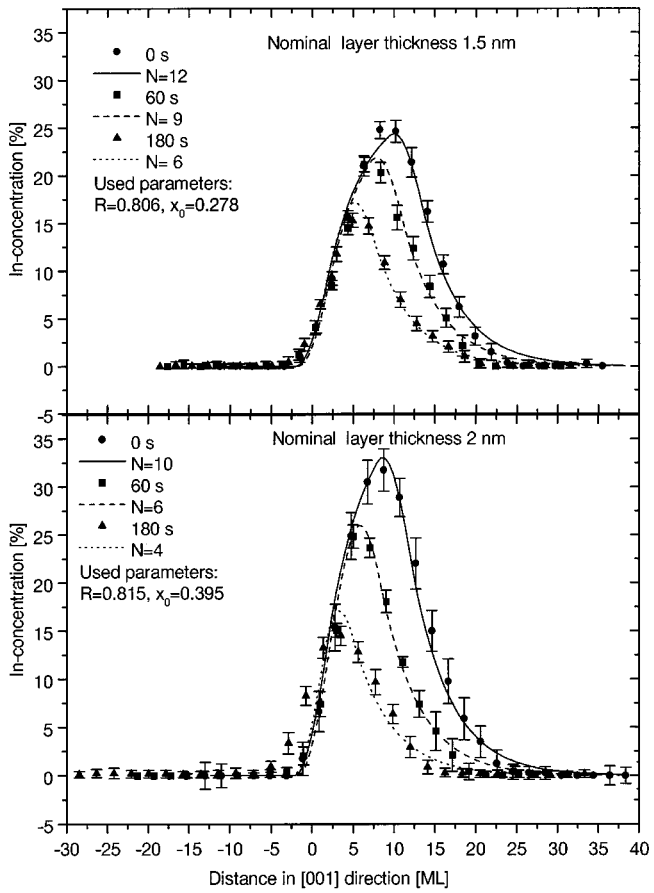

FIG. 12. Concentration profiles in growth direction plotted versus the distance in the [001] direction. The profiles were obtained by averaging along the (002) planes in approximately 3-nm-wide regions *of the wetting layer*. The dots, squares, and triangles represent the experimental data. The error bars are calculated from the mean deviation of averaged values. The zero point of the abscissa corresponds to the interface between GaAs buffer and the $In_xGa_{1-x}As$ layer. The solid, dashed, and dotted curves are fit curves calculated according to the phenomenological Muraki formula for segregation. The meaning of the listed fit parameters N, R, and x_0 is explained in the text.

interruption. The profiles are not symmetrical but show a slower decay towards the GaAs cap layer. This is a clear indication for segregation. The area below each curve yields the total amount of In that is contained in the wetting layer. Figure 13 illustrates its behavior in dependence of the duration of the growth interruption. For both samples with 1.5 and 2 nm layer thickness, the amount of In contained in the wetting layer can be described by an exponential decay. The time constant τ (see caption of Fig. 13) of the 1.5 nm samples is 1.5 times larger than that of the 2 nm samples. The extrapolation of the exponential fit curves towards longer growth interruption approaches an asymptotic value corresponding to 2.2 ML $In_{0.6}Ga_{0.4}As$.

V. DISCUSSION AND CONCLUSIONS

In the previous section we found that the ''wetting layer'' between the islands of capped samples significantly differs from the wetting layer that was observed in the uncapped sample. In the latter case we found 3D islands with a height

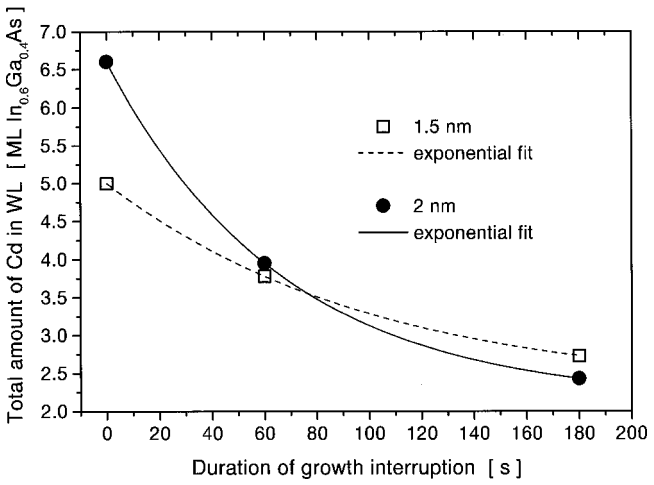

FIG. 13. Total amount of In X_{sum} that is contained in the wetting layer, plotted versus the duration of the growth interruption t. The solid and dashed lines represent exponential fit curves calculated according to $X_{\mathrm{sum}}[\mathrm{ML\ In_{0.6}Ga_{0.4}As}]=X_0+C\exp(-t/\tau)$. The fit parameters are $X_0=2.27$, $C=2.73$, $\tau=101.6$ for the 1.5 nm samples and $X_0=2.13$, $C=4.47$, $\tau=66.8$ for the 2 nm sample.

of approximately 11 ML (see Fig. 4) measured from the wetting-layer surface. The strain state analysis of an uncapped island revealed indications for an approximately 1 or 2-ML-thick wetting layer. On the other hand, the investigations of the capped islands unambiguously show an approximately 15-ML-thick ''wetting layer'' that contains islands as In-rich insertions. Here we deduce a growth model that explains the observed morphological transformation of the wetting layer during the overgrowth with GaAs.

A. Bulk Interdiffusion

Generally, the interdiffusion of In in GaAs could lead to a broadening of the $In_xGa_{1-x}As$ layer. The diffusion coefficient is $D=1.6\times10^{-24}$ cm^2/s for the growth temperature of 500 °C.[18] We assumed a Heaviside function for the initial concentration profile $x(t,z)$, where t is the duration of the diffusion process and z is the coordinate in growth direction. By calculating a solution for the linear diffusion equation

$$\frac{\partial x(t,z)}{\partial t}=D\frac{\partial^2 x(t,z)}{\partial z^2}, \tag{6}$$

we found that the effect of interdiffusion is negligible here because t is of the order of only a few min.

Additionally, it is conceivable that the strain has an effect on the diffusion in strained layer heterostructures. In Ref. 19 the effect of strain was taken into account by regarding the strain energy as a contribution to the activation energy of the diffusion process. The authors found that the effect of strain is negligible in an $In_xGa_{1-x}As$/GaAs heterostructure at temperatures below 600 °C. It is appropriate to note that the interdiffusion during the ion-milling process (performed as the final stage of the TEM-specimen preparation) is also negligible because the specimen heating is well below 300 °C.[20]

B. Segregation

The segregation of In at the growth surface is a well-known effect in $In_xGa_{1-x}As$. Moison *et al.*[7] deduced a model for the segregation by introducing a characteristic energy E_S for the movement of an atom from the bulk to the surface. Their approach involves the entropy term, the ''chemical'' energy E_S, and a term corresponding to the pseudomorphic elastic strain energy term as contributions to the free energy. They found a value of $E_S=0.15\pm0.1$ eV by x-ray photoelectron spectroscopy (XPS) for the segregation of In in $In_xGa_{1-x}As$. Later on, Gerard and Marzin[21] obtained $0.15\ \mathrm{eV}\leqslant E_S\leqslant 0.2$ eV by PL. Nagle *et al.*[22] found that the segregation efficiency is not only sensitive on the growth temperature but also much more on the V/III flux ratio. They observed that a reduction of the As_4 flux by a factor of 3 increases E_S to 0.40 eV at a growth temperature of 530 °C.

The phenomenological description of the segregation, that we will use here, is based on a suggestion of Muraki *et al.*[23] They assumed that a certain fraction R of In atoms on the topmost layer segregate into the layer grown on top. According to their model, the In concentration in the nth ML is given in the form

$$x_n=\begin{cases}0: & n<0\ \ (\mathrm{buffer})\\ x_0(1-R^n): & 0\leqslant n\leqslant N\ \ (\mathrm{well})\\ x_0(1-R^N)R^{n-N}: & n>N\ \ (\mathrm{cap})\end{cases} \tag{7}$$

where x_0 is the nominal In concentration and N is the nominal layer thickness in monolayers. In the literature we find several values for R measured in MBE grown $In_xGa_{1-x}As$. At a growth temperature of 500 °C, the values are 0.88 (Ref. 23) (V/III=4), 0.84 (Ref. 23) (V/III=12), 0.8,[24] and 0.75.[25] At 520 °C, published values include 0.84 (Ref. 26) and 0.8.[27]

To be able to compare the values found in the literature with our measurement, Eq. (7) was fitted to the experimentally observed concentration profiles in growth direction depicted in Fig. 12. The parameters x_0, R, and N were used as fit parameters. A tilt of the specimen of 4° toward the exact zone-axis orientation was taken into account. Figure 12 also contains the resulting fit curves and the corresponding values of the fit parameters. It is appropriate to note that the ascending part of the concentration profiles mainly defines x_0 whereas the descending part prescribes R. In agreement with the data found in the literature, all curves are well fitted with $R=0.810\pm0.006$. The fit values for x_0 are 0.278 and 0.395 for the 1.5 nm and 2 nm samples, respectively. Note that x_0 has been kept constant for samples with the same $In_xGa_{1-x}As$ layer thickness. This was found to be a good approximation for all measured profiles of specimens with 0 and 60 s growth interruption. In the samples with 180 s interruption, a tendency to smaller values $x_0\approx0.2$ was observed. Obviously, all fitted values for x_0 significantly deviate from the ''real'' nominal In concentration of 0.6. According to Eq. (7), the values for N describe the nominal $In_xGa_{1-x}As$ layer thickness, i.e., the number of monolayers that were grown under In flux. The fitted values are approximately $N=11$ for the samples without growth interruption, in clear contradiction to the nominal thicknesses of 5 and 7 ML for the 1.5 and 2 nm samples, respectively. Taking into account that the concentration profiles were measured in the

wetting-layer regions between the islands, we would expect values for N that are approximately equal to the wetting-layer thickness of 1 to 2 ML observed in uncapped samples.

C. Resulting growth model

(a) *Summary of experimental observations.* We showed in the previous sections that the significant broadening of the ''wetting layer'' in capped layers to approximately 15 ML cannot be due to bulk interdiffusion. The concentration profiles can be well fitted by the phenomenological model for segregation given in Eq. (7). The descending parts of the measured concentration profiles define the fitted values for R that are in good agreement with data that we found in the literature. However, the width of the ascending parts of the profiles (described by the fit parameter N) as well as its slope (described by x_0) deviate from the expected values. Additionally, Fig. 13 reveals a total amount of In in the wetting layers of the samples with 0 s growth interruption corresponding to 6.5 ML $In_{0.6}Ga_{0.4}As$ (2 nm sample) and 5 ML $In_{0.6}Ga_{0.4}As$ (1.5 nm sample). These values are significantly larger than the maximum amount of 2 ML $In_{0.6}Ga_{0.4}As$ determined for the wetting layer in uncapped samples.

(b) *Incorporation of migrating In.* We show now that our measurements can well be explained by taking into account the migration of In along the growth surface as well as strain-induced migration of Ga. Evidence for the migration of In was already obtained in Sec. IV B 1 where we observed an instability of the coherent islands. The morphology change cannot be due to bulk interdiffusion that is not effective at a growth temperature of 500 °C. Therefore, the dissolution of the coherent islands generates a current of In-atoms migrating along the sample surface. The current of In-atoms also persists during the growth of the cap layer resulting in the presence of In atoms migrating on top of the prevailing growth surface of the cap. The migrating In atoms can be incorporated into the growing cap layer. The unstable islands have to be regarded as a source of In atoms that are active even if the In flux from the Knudsen cells are turned off. Therefore, the overall amount of In atoms contained in the wetting layer is expected to be larger in the capped samples than in the uncapped samples. Here it is appropriate to note that the migrating In is transported toward the large strain-relaxed In(Ga)As islands that act as a sink for In atoms. Experimental evidence for this process is given in Fig. 7 where the density of strain-relaxed islands increases with increasing duration of the growth interruption.

(c) *Interpretation of the parameter* x_0. The parameter x_0 of the fit curve [Eq. (7)] describing its ascending part mainly depends on the amount of In atoms migrating along the growth surface. In Sec. IV B 1 we found that the density of coherent islands drops much quicker in the 2 nm samples than in the 1.5 nm samples. Therefore, we have to deduce that the current of migrating In atoms is larger for the 2 nm sample during the first 60 s of the growth interruption where we find a decreasing density of the coherent islands (see Fig. 7). Consequently, we expect a larger value of x_0 for the 2 nm sample, which indeed can clearly be observed in Fig. 12 where we find $x_0 = 0.28$ for the 1.5 nm sample and $x_0 = 0.40$ for the 2 nm sample. Coherent islands were not observed in the sample with 2 nm $In_xGa_{1-x}As$ layer thickness and 180 s growth interruption. This explains the reduced slope for the ascending part of the corresponding concentration profile (see the triangles in the lower part of Fig. 12). In this case, the profile results from a combination of initial wetting layer, exchange of In atoms inside the wetting layer with the surface during the growth interruption, remaining migrating In atoms from dissolved coherent islands, and In atoms exchanged between large strain-relaxed islands.

(d) *Strain-induced migration of Ga.* In Figs. 10 and 11 it is conspicuous that the upper interface of the $In_xGa_{1-x}As$ layer appears flat. Therefore, we have to explain why the incorporation of migrating In only takes place in between the islands and not on top of them. It can be seen in Fig. 9 that the cap layer does not grow on top of strain-relaxed islands. This effect was also observed by Qianghua Xie *et al.*[28] where the authors found an island-induced strain-driven adatom migration during the GaAs cap layer growth by the placement of very thin $Al_xGa_{1-x}As$ marker layers. They found that the growth rate of the GaAs cap layer depends on the local in-plane lattice parameter at the growth surface and on the growth temperature. The elastic relaxation of the coherent islands or the plastic relaxation of incoherent islands yields an enlarged in-plane lattice parameter on top of the islands. If the surface mobility of the Ga atoms is large enough ($T_G \geqslant 480$ °C), the Ga atoms migrate from the top of the islands toward the regions between the islands. Therefore, the growth rate of the cap layer is significantly larger in between the islands.

(e) *Interpretation of the parameter N.* The coherent islands can only act as sources for In atoms as long as the cap layer is thinner than their height. The additional flux of In atoms will stop as soon as the coherent islands are covered by the GaAs. Therefore, the parameter N in Fig. 12 should be correlated with the height of the islands. This supposition can be easily checked for the capped samples without growth interruption where we find $N \approx 11$ ML, in good agreement with the mean height of 10 ML of the coherent islands observed in uncapped samples (see Sec. IV A and Fig. 4). Figure 12 indicates that the height of the coherent islands decreases with increasing duration of the growth interruption. This behavior seems plausible because the dissolution of an island takes place at its surface, which reduces its height.

(f) *Correlation with the PL.* In Fig. 8, the large FWHM of the sample with 2 nm $In_xGa_{1-x}As$ layer thickness and a growth interruption of 60 s is conspicuous. From this observation we would deduce a broad variation of the island sizes and/or the In concentration inside the islands. Indeed, this expectation is confirmed in Fig. 10(e) where one can see small islands with low In concentration and larger islands with high In concentration. In accordance with the PL data, Fig. 10(e) exhibits the largest differences in the sizes as well as the In concentrations of the islands.

(g) *Composition distribution in free-standing islands.* Theoretical considerations of the SK growth of islands during alloy deposition carried out by Tersoff[29] suggest that the islands nucleate at a substantially different composition than the alloy layer. Note that this statement refers to the critical nucleus that is generally much smaller than the final island. During island growth, the wetting layer constitutes a reservoir of In atoms that feeds the islands. He pointed out that the growth of the islands takes place at the expense of the

film if the incident flux of In atoms is turned off. The compositional enrichment of the islands leaves behind a compositionally depleted film. This consideration would explain our strain state analysis measurements where we could not find indications for a wetting layer between the islands in uncapped samples. The bottom ML of the island containing 20% In (see. Fig. 4) could reflect the wetting layer during the earliest stage of the growth, which was frozen in the island. Tersoff discussed a possible ''self-capping'' of quantum dots that would result in islands with high In concentration in the center surrounded by material with lower concentration. In our experiments we do not find indications for ''self-capping.'' Instead, the In concentration increases from the bottom to the top of the island (see. Fig. 4). We suppose that the segregation and strain-induced migration[28] of In and Ga that was discussed in the preceding is the main effect that defines the composition distribution inside the island. During the initial growth of an island (first ML), the in-plane lattice parameter of the island adapts to the lattice parameter of the substrate. With proceeding growth of the island, the degree of elastic relaxation and, therefore, the in-plane lattice parameter increase. Due to the strain-induced migration of In and Ga, the local composition of the currently growing ML M of the island depends on the in-plane lattice parameter of the ML $M-1$. Therefore, the degree of elastic relaxation of the island that increases from the bottom to the top of the island induces a composition distribution also increasing from bottom towards the top of the island.

VI. SUMMARY

In this paper we presented a detailed TEM investigation of the structure and chemical morphology of free-standing and capped $In_{0.6}Ga_{0.4}As$ layers with nominal thicknesses of 1.5 and 2 nm in dependence of growth interruptions of 0, 60 and 180 s duration that was introduced prior to the cap layer growth. In uncapped samples, we found two kinds of islands. Coherent islands with a diameter of approximately 13 nm and large plastically strain-relaxed islands. In the case of the coherent islands, the In concentration increases from the bottom to the top. In our opinion, the In distribution inside the islands is mainly determined by the segregation and the strain-induced migration of In and Ga. Due to the strain-induced migration, the In concentration of a growing ML M depends on the in-plane lattice parameter of the ML $M-1$. We did not find indications for a wetting layer in regions beside the islands. This observation could be explained by a decomposition-induced depletion of the wetting layer between the islands.[29] The strain field inside the islands allowed an estimate for the wetting-layer thickness of 1–2 ML during the very initial stage of the growth.

In capped samples, the density of coherent islands decreases (more quickly for the 2 nm sample) with increasing duration of the growth interruption. The density of dislocated islands increases. The chemical morphology of the capped samples significantly deviates from uncapped samples. The structure of the $In_xGa_{1-x}As$ layer can be described as an about 4-nm-thick quantum well with (rather) homogeneous thickness containing approximately 13-nm-large inclusions with enhanced In concentration. The morphology transformation during the cap layer growth was explained by the interplay of mainly three effects. First, the instable coherent islands are a source for In atoms that are transported to the large dislocated islands via migration along the growth surface. The migrating In atoms are incorporated into the growing cap layer. Second, the strain-induced migration of Ga causes a significantly reduced growth rate of the GaAs cap layer on top of the elastically strain-relaxed islands. Therefore, the cap layer preferentially fills the regions between the islands. Third, segregation occurs leading to a protraction of In. The measured concentration profiles yield a segregation probability of $R=0.810\pm0.006$ at a temperature of 500 °C that is in good agreement with published data.

ACKNOWLEDGMENT

This work was supported by the Deutsche Forschungsgesellschaft under Contract No. Ro 2057/1.

[1] Y. Arakawa and H. Sakaki, Appl. Phys. Lett. **40**, 939 (1982).
[2] M. Grundmann, O. Stier and D. Bimberg, Phys. Rev. B **52**, 11 969 (1995), and references therein.
[3] A. Rosenauer, U. Fischer, D. Gerthsen and A. Förster, Appl. Phys. Lett. **71**, 3868 (1997).
[4] D. Bimberg, M. Grundmann, and N.N. Ledentsov, *Quantum Dot Heterostructures* (Wiley, Chichester, England, 1999).
[5] H.T. Dobbs, D.D. Vvedensky, and A. Zangwill, Appl. Surf. Sci. **123/124**, 646 (1998), and references therein.
[6] S. Ruvimov, Z. Liliental-Weber, N.N. Ledentsov, M. Grundmann, D. Bimberg, V.M. Ustinov, A. Yu. Egorov, P.S. Kop'ev, Zh.I. Alferov, K. Scheerschmidt, and U. Gösele, in *Compound Semicondutor Electronics and Photonics*, edited by R.J. Shul, S.J. Pearton, F. Ren, and C.-S. Wu, MRS Symposia Proceedings No, 421 (Materials Research Society, Pittsburgh, 1996), p. 133.
[7] J.M. Moison, C. Guille, F. Houzay, F. Barthe, and M. Van Rompay Phys. Rev. B **40**, 6149 (1989).
[8] A. Rosenauer, S. Kaiser, T. Reisinger, J. Zweck, W. Gebhardt, and D. Gerthsen, Optik (Stuttgart) **102**, 63 (1996).
[9] M.M.J. Treacy and J.M. Gibson, J. Vac. Sci. Technol. B **4**, 1458 (1986).
[10] A. Rosenauer, T. Remmele, and D. Gerthsen, Optik (Stuttgart) **105**, 99 (1997).
[11] A. Ourmazd, P. Schwander, C. Kisielowski, M. Seibt, F.H. Baumann, and Y.O. Kim, in *Microscopy of Semiconducting Materials 1993*, Proceedings of the Royal Microscopical Society Conference (Institute of Physics, London, 1993), p. 1.
[12] C. Kisielowski, P. Schwander, F.H. Baumann, M. Seibt, Y.O. Kim, and A. Ourmazd, Ultramicroscopy **58**, 131 (1995).
[13] A. Rosenauer and D. Gerthsen, Adv. Imaging Electron Phys. **107**, 121 (1999).
[14] P.A. Stadelmann, Ultramicroscopy **51**, 131 (1987).
[15] A. Rosenauer, U. Fischer, D. Gerthsen, and A. Förster, Ultramicroscopy **72**, 121 (1998).
[16] A. Rosenauer and D. Gerthsen, Ultramicroscopy **76**, 49 (1998).
[17] A. Rosenauer, N. Peranio, and D. Gerthsen, in *Microscopy of*

Semiconducting Materials 1999, Oxford, UK, 1999, Proceedings of the Royal Microscopical Society Conference, edited by A.G. Cullis and J.L. Hutchison (Institute of Physics Publishing, London, 1999), No. 164, p. 117.
[18] O.M. Khreis, W.P. Gillin, and K.P. Homewood, Phys. Rev. B **55**, 15 813 (1997).
[19] W.P. Gillin and D.J. Dunstan, Phys. Rev. B **50**, 7495 (1994).
[20] G. Lu, Philos. Mag. Lett. **68**, 1 (1993).
[21] J.M. Gerard and J.Y. Marzin, Phys. Rev. B **45**, 6313 (1992).
[22] J. Nagle, J.P. Landesmann, M. Larive, C. Mottet, and P. Bois, J. Cryst. Growth **127**, 550 (1993).
[23] K. Muraki, S. Fukatsu, Y. Shirakia, and R. Ito, Appl. Phys. Lett. **61**, 557 (1992).
[24] R. Kaspi and K.R. Evans, Appl. Phys. Lett. **67**, 819 (1995).
[25] M. Ilg and K.H. Ploog, Phys. Rev. B **48**, 11 512 (1993).
[26] H. Toyoshima, T. Niwa, J. Yamzaki, and A. Okamoto, J. Appl. Phys. **75**, 3908 (1994).
[27] M. Leroux, N. Grandjean, C. Deparis, J. Massies, C. Lopez, R. Mayoral, and F. Meseguer, Jpn. J. Appl. Phys., Part 1 **34**, 3437 (1995).
[28] Qianghua Xie, P. Chen, and A. Madhukar, Appl. Phys. Lett. **65**, 2051 (1994).
[29] J. Tersoff, Phys. Rev. Lett. **81**, 3183 (1998).